PAPER

Check for updates

Enhanced sintering resistance of bimetal/SBA-15 catalysts with promising activity under a low temperature for CO methanation†

Miao Tao,[a] Changlu Zhou,[a] Yaoqi Shi,[ab] Xin Meng, [ID] [ab] Jia Gu,[a] Wenli Gao[a] and Zhong Xin [ID] *[ab]

According to its thermodynamic equilibrium analysis and strong exothermic characteristics, the major challenge of syngas methanation is to develop a high-efficient low-temperature catalyst with superior sintering resistance. In this study, bimetal-based SBA-15 catalysts were prepared *via* a citric acid-assisted impregnation method and applied in CO methanation. The obtained catalysts were characterized *via* X-ray diffraction, N_2 adsorption−desorption, high-resolution transmission electron microscopy, X-ray photoelectron spectroscopy, H_2 temperature-programmed reduction and other techniques. Combining the structural characterization of the fresh and used catalyst, the function of the organic additive and metal promoters was revealed. The catalysts exhibited superior low-temperature activity and excellent sintering resistance owing to the electron migration from the additive metal to Ni, strong interaction between the metal and support and the confinement effect of the support. The catalyst with Mo as a promotor exhibited the best dispersion and the largest surface concentration of nickel, which resulted in its highest catalytic activity among the catalysts. The design and preparation of a highly effective catalyst can provide novel insight into the preparation of other catalysts.

1 Introduction

The past several decades have witnessed a boom in the global economy. Fast transportation, convenient electricity, and modern materials with the consumption of fossil energy make it easier and cozier for humans to live on Earth. However, society is beginning to realize that great achievements today seem to be at the price of destroying nature by severe environmental issues. Recently, the adverse health impacts of air polluted with fine particulate matter ($PM_{2.5}$, particulate matter with a mean aerodynamic diameter of 2.5 μm or less) have attracted increasing attention around the world, which has become the fifth leading cause of death in China with 900 000 premature deaths each year since 2013. Therefore, the Air Pollution Prevention and Control Action Plan was released by China's Ministry of Ecology and Environment, several other central government departments and the governments of six provincial-level regions in March 2017 in order to improve air quality.[1] The plan embedded a large-scale "coal-to-gas" reform

program in 28 cities. Consequently, the shortage of natural gas supplies is growing and the gap between supply and demand will be 200 billion m^3 by 2020.[2] Therefore, the development of coal-to-SNG (substitute natural gas) can not only realize the clean utilization of abundant coal resources in China but also meet the rapid growth in the demand for natural gas.[3,4]

Although methanation reactions are thermodynamically favorable, a catalyst is necessary to obtain an appropriate rate, especially for the system to deal with carbon monoxide at relatively high concentrations.[5] Ni-based catalysts are one of the most widely studied and applied catalysts in CO methanation reactions to produce SNG due to their high performance-cost ratio.[6,7] However, although Ni catalysts are favored in the CO methanation reaction, it is a big challenge to prepare highly efficient catalysts to accurately control the dispersion and structural properties of the surface Ni species.[8] Besides, the strong exothermic reaction and thermodynamic equilibrium analysis of this process indicate that a lower reaction temperature is beneficial for syngas methanation.[9] More importantly, a large temperature increase (hot spots can reach 600–700 °C) in modern SNG processes with high CO concentrations accelerates the sintering and coking of the catalyst.[10] Therefore, it is urgent to develop high-efficient low-temperature catalysts for syngas methanation with excellent high-temperature stability *via* a simple method.

In our previous work, SBA-15 worked as good support to improve the Ni dispersion and catalytic performance.[11]

[a]Shanghai Key Laboratory of Multiphase Materials Chemical Engineering, East China University of Science and Technology, People's Republic of China. E-mail: xzh@ecust.edu.cn

[b]State Key Laboratory of Chemical Engineering, School of Chemical Engineering, East China University of Science and Technology, Shanghai, People's Republic of China

† Electronic supplementary information (ESI) available. See DOI: 10.1039/d0ra02168g

Paper

However, the nickel particles easily agglomerated under operation at high temperature due to the weak interaction between the metal and support, which has a negative effect on the catalytic performance. Recently, bimetal catalysts exhibited good catalytic ability owing to the enhancement of the metal-support interaction and electronic effect. Studies have shown that noble metals (Ru[12] and Pt), transition metals (Mo and Fe[13]) and rare earth metals (La[14] and Ce[15]) can improve the performance of Ni-based catalysts *via* electronic or structural effects. Ryuji Kikuchi *et al.*[16] prepared Ru–M/TiO$_2$ catalysts doped with different metals (M = Ni, Co, Fe, La and K) and they found that the introduction of Co and La improved both the CO and CO$_2$ methanation activity. Our previous study found[17] that the introduction of molybdenum could enhance the interaction between Ni and the support, resulting in an improvement of the heat resistance of Ni-based methanation catalysts. In addition, the introduction of lanthanum[18] can improve the nickel dispersion and performance of Ni-based catalysts, thereby effectively enhancing their activity and anti-coking ability. The Ni–Fe–Al xerogel exhibited better catalytic performance than that of the Ni–Al xerogel for CO$_2$ methanation at a low reaction temperature in the study by Hwang *et al.*[19] The promoting effect of the additive metal depends not only on its own electronic structure but also on its distribution on the surface of the support. Although many efforts have been dedicated to the synthesis of bimetallic composites, most of the synthetic processes are expensive and complicated. Therefore, there is still a need to develop simple methods to obtain highly dispersed bimetallic oxides in the channels of mesoporous silica with high activity at low temperature.

In this work, we used mesoporous silica SBA-15 as the support to improve the nickel dispersion, metals (Mo, La and Fe) as promoters to change the physicochemical properties of the active sites and a citric acid-assisted impregnation method to induce the metals to enter the channels of SBA-15. The physicochemical properties of the bimetal catalysts were determined by X-ray diffraction (XRD), N$_2$ adsorption–desorption, high-resolution transmission electron microscopy (HRTEM), X-ray photoelectron spectroscopy (XPS), H$_2$ temperature-programmed reduction (H$_2$-TPR), H$_2$ pulse chemisorption, CO temperature-programmed desorption (CO-TPD), thermogravimetry (TG) and elemental analysis. Then, CO methanation was employed as a probe reaction to evaluate the catalytic activities of the samples. Combining the structural characterization of the fresh and used catalysts with their catalytic performances, the effects of citric acid and the metal promoters were studied.

2 Experimental

2.1 Catalyst preparation

Poly(ethylene glycol)-*block*-poly(propylene glycol)-*block*-poly(-ethylene glycol) (P123) of molecular weight 5800 was obtained from Sigma-Aldrich Corporation, USA. Tetraethyl orthosilicate (TEOS), hydrochloric acid with a concentration of 36–38% and citric acid were purchased from Shanghai Lingfeng Chemical Reagent Co., Ltd, China. Ni(NO$_3$)$_2$·6H$_2$O, La(NO$_3$)$_3$·nH$_2$O,

Fe(NO$_3$)$_3$·9H$_2$O and ammonium molybdate (analytical grade) were provided by Sinopharm Chemical Reagent Co., Ltd, China. All reagents were utilized directly without further purification.

The SBA-15 support was synthesized using the general approach first described by Stucky and co-workers.[20] P123 was the template and TEOS was the Si precursor. The bimetal-based SBA-15 catalysts were prepared *via* a citric acid (CA)-assisted impregnation method. 1.0 g SBA-15 powder was dispersed in an aqueous solution containing the required amount of Ni(NO$_3$)$_2$·6H$_2$O and additive metal precursors. The mixture was put in an ultrasonic cleaner for 30 min, dried at 50 °C under vacuum for 12 h, and finally calcined at 500 °C for 5 h (1 °C min^{-1} heating rate). The obtained catalysts were labeled as M-Ni/S15-CA, where M represents the additive metal. On the contrary, Ni/S15 prepared by the traditional impregnation method without citric acid and Ni/S15-CA prepared without additive metal were used as the control.

2.2 Characterization

The surface area, pore volume and average pore size of the catalysts were measured using N$_2$ adsorption–desorption with a Micromeritics ASAP 2000M analyzer, USA. Prior to the test, the samples were degassed at 300 °C for 4 h. The surface area (S_{BET}) was calculated according to the Brunauer–Emmett–Teller (BET) method in the relative pressure (p/p_0) range of 0.05–0.35. The pore size distribution was calculated using the Barret–Joyner–Halenda (BJH) method using the desorption branch, which was based on capillary condensation. The pore volume (V) refers to the volume of nitrogen adsorbed when P/P_0 is 0.995.

X-ray diffraction (XRD) was used to investigate the structure of SBA-15 and the crystalline phases of the metal particles on the catalysts. The XRD patterns were obtained with a Bruker D8 Advance X-ray diffractometer (Germany) using Ni-filtered Cu radiation at 40 kV. The sizes of the crystalline metal particles were determined using the Scherrer equation.

The H$_2$-temperature-programmed reduction (H$_2$-TPR), H$_2$ pulse chemisorption, and temperature-programmed desorption (TPD) of CO were measured using a Micromeritics AutoChem II 2920 adsorption instrument, USA. TPR: 20 mg sample was initially purged with high purity Ar at a flow rate of 30 mL min^{-1} at 200 °C for 2 h to remove the moisture and impurities. A stream of 10% H$_2$/Ar was then switched to the catalyst while the temperature was increased at a rate of 10 °C min^{-1} to 700 °C. The hydrogen consumption was detected by a thermal conductivity detector. H$_2$ pulse chemisorption: the catalyst was first reduced at 500 °C in a hydrogen atmosphere (50 mL min^{-1}) for 2 h and then pretreated in He for 1 h at 200 °C. After cooling to room temperature in Ar, 10% H$_2$/Ar pulse adsorption was performed at 40 °C 10 times. TPD: the catalyst sample was pretreated in He for 1 h at 200 °C. After cooling to room temperature in Ar, 10% CO/Ar was introduced at 40 °C for 1 h. The catalysts were then purged with 30 mL min^{-1} He for 1 h to remove the physically adsorbed CO. The desorption curve was obtained by increasing the temperature from 50 °C to 500 °C under a pure Ar flow.

High-resolution transmission electron microscopy (HRTEM) was a simple way to analyze the structure of the catalysts and their metal distribution. The images were obtained with a JEM-2100F field emission electron microscope, Japan. Prior to observation, the samples were directly suspended in ethanol under ultrasonication. A copper grid was dipped into the resulting suspension and dried at room temperature.

The X-ray photoelectron spectroscopy (XPS, PerkinElmer, PHI 5000C ECSA, USA) with monochromatic Al Kα radiation (1486.6 eV) was used to measure the electron state of the metal on the surface of the catalysts. The C 1s peak at 284.8 eV was taken as a reference for binding energy (BE) calibration and the Shirley model was selected as the background subtraction method.

The contents of nickel and metal promoters in the catalysts were tested by inductively coupled plasma spectroscopy (Vanan 710, USA). The samples were dissolved in KOH and hydrofluoric acid.

Thermogravimetric (TG) and elemental analysis were used to measure the carbon amount on the catalysts. TG was performed with an SDT Q-600 instrument (USA) under an air flow from 50 °C to 800 °C at a heating rate of 10 °C min^{-1}. A Vario EL III elemental analyzer from Elementar (Germany) was used.

2.3 Catalytic activity evaluation

The catalytic performance evaluation was carried out in a fixed-bed stainless steel reactor. In each experiment, 0.4 g of catalyst (sieve fraction 100 mesh) and 3 g quartz sand (50–80 mesh) were added to the reactor. N$_2$ (99.999%) was introduced in the reactor at a flow rate of 20 mL min^{-1} for 30 min to remove the air and the reactor was heated at a rate of 10 °C min^{-1} from room temperature to 500 °C. Before the reaction, the catalyst was reduced by H$_2$ (99.999%) with 50 mL min^{-1} for 2 h and then cooled to 250 °C in an N$_2$ atmosphere. Subsequently, the syngas of H$_2$ (60 mL min^{-1}) and CO (99.95%, 20 mL min^{-1}) was switched as the feed gas to synthesize methane at 0.1 MPa with the weight hourly space velocity of 15 000 mL g^{-1} h^{-1}. The products from the reactor went through a gas–liquid separator, and the outlet gas was quantitatively analyzed by an on-line gas chromatograph (Techcomp, GC7890T, China), which was equipped with a thermal conductivity detector (TCD) and flame ionization detector (FID), using Ar as the carrier gas. The equations used for calculating the CO conversion and CH$_4$ selectivity are as follows:

$$CO \ conversion(\%) = \frac{F(CO_{in}) - F(CO_{out})}{F(CO_{in})} \times 100\%$$

$$CH_4 \ selectivity(\%) = \frac{F(CH_{4,out})}{F(CO_{in}) - F(CO_{out})} \times 100\%$$

where F represents the flow of CO and CH$_4$ (mL min^{-1}, STP).

3 Results and discussion

3.1 Metal dispersion enhancement in the catalysts

Generally, the N$_2$ adsorption–desorption curve of the mesoporous material SBA-15 is a type IV isotherm (according to the IUPAC classification). Capillary condensation in the mesopores causes a sharp increase in the adsorption isotherm under the corresponding pressure. Thus, a dramatic increase in the adsorption isotherm reflects the regularity of the pore size. The N$_2$ adsorption–desorption isotherms and pore size distribution of all the catalysts are presented in Fig. S1.† It is obvious that all the samples exhibited the typical type IV isotherms with an H1 hysteresis loop, which reflects the uniform distribution of the cylindrical pores with two open ends. In the low-pressure section, N$_2$ molecules are adsorbed on the inner surface of the mesopores from monolayer to multilayer, resulting in a slow increase in the adsorption capacity. In addition, all samples have a similar increasing trend in the relative pressure range of 0.6 to 0.9, indicating that the incorporation of active components and organic additives had little impact on the ordered structure of the support. The pore size distribution curves in Fig. S1(B)† show narrow peaks at about 8.6 nm and 1.6 nm, suggesting a certain amount of micropores besides mesoporous in the catalyst. The detailed textural parameters of the catalysts are listed in Table S1.† SBA-15 has a pore volume of 1.21 cm^3 g^{-1} with a BET surface area of 838 m^2 g^{-1} and its micropores surface area and volume are 118 m^2 g^{-1} and 0.04 cm^3 g^{-1}, respectively. After loading Ni element, the BET surface area, microporous surface area, pore volume and average pore diameter of the catalysts decreased significantly to 689 m^2 g^{-1}, 96 m^2 g^{-1}, 1.00 cm^3 g^{-1}, and 0.03 cm^3 g^{-1}, respectively. Moreover, these parameters further decreased with the incorporation of other metal elements (Mo, La, and Fe) and citric acid (CA). For instance, the BET surface area of Mo–Ni/S15-CA decreased from 838 to 659 m^2 g^{-1} and the pore volume declined from 1.21 to 0.96 cm^3 g^{-1}. The occupation of these active species in the pores should be the reason for the reduction in the textural parameters of the catalysts, which was further confirmed by high-resolution transmission electron microscopy (HRTEM), as shown in Fig. 1. The NiO particles can be observed as black spots in Fig. 1(A) with a wide size distribution of 8–30 nm, which are distributed outside the pores of the support due to the transportation and redispersion of metal ions during the evaporation process. After the incorporation of CA and the additive metal, the particle size of NiO became much smaller, and it is uniformly dispersed inside the pores of the carrier in the HRTEM images. The EDS curves confirmed the presence of nickel and the metal promoters. The low peak intensity of the additive metal is due to its relatively small content in the catalyst and Cu was also detected owing to the copper microscope grid for supporting the samples during the measurements. The better distribution of metallic nickel in the catalyst was verified by the elemental mapping of Ni/S15-CA from HRTEM in Fig. 1(F). The Si and O elements were uniformly distributed in the measured area, while metallic nickel was evenly distributed according to the nano-pore array. This is because citric acid decreases the interfacial tension of the impregnation solvent so that the redispersion of metal ions in the drying process is hindered during preparation, resulting in the uniform distribution of the metal species inside the pores of the support.

The mesoporous structure and metal dispersion of the catalyst were also characterized by XRD. Three obvious
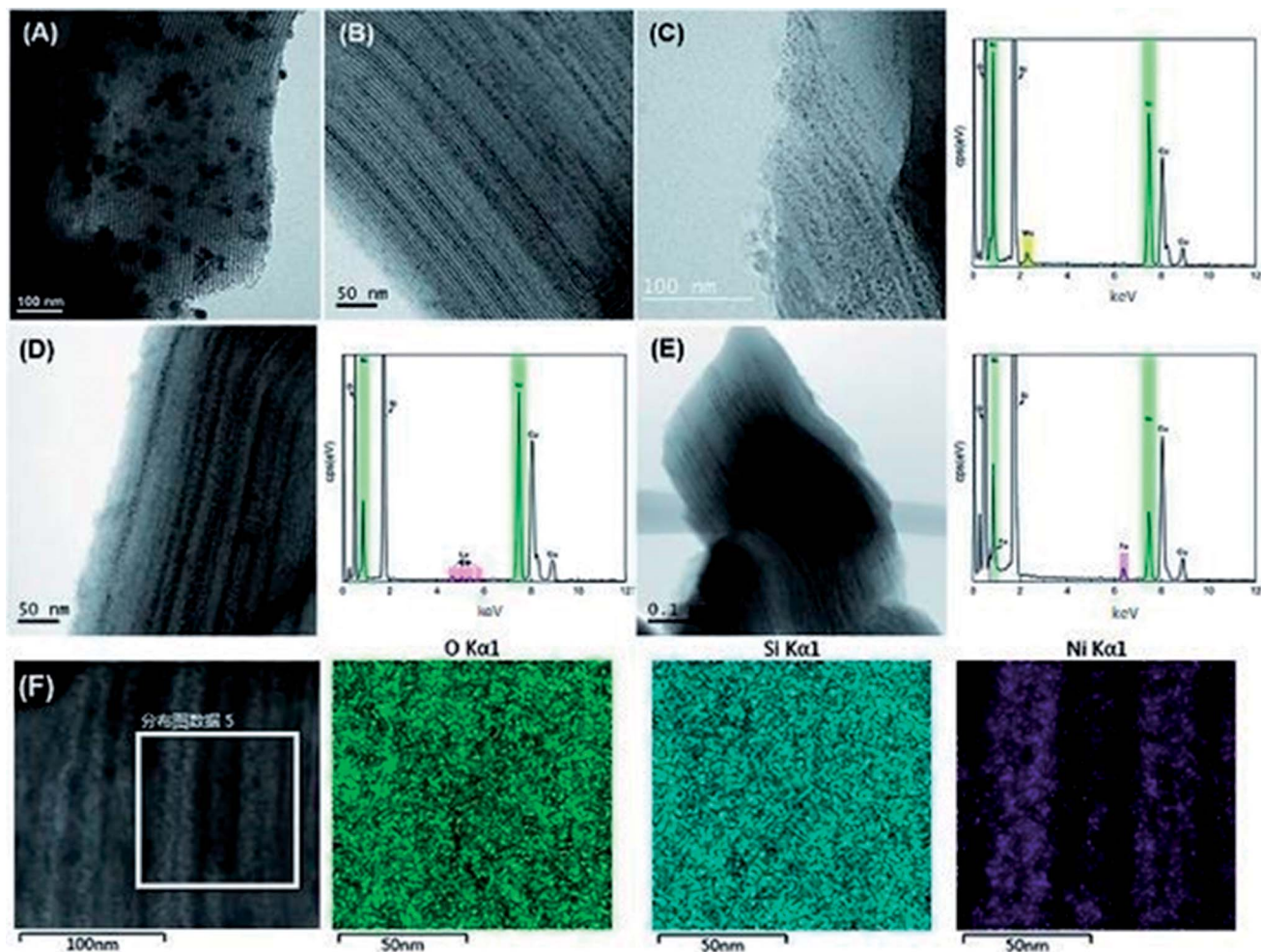
Fig. 1 HRTEM-EDS images of the fresh catalysts. (A) Ni/S15, (B) Ni/S15-CA, (C) Mo−Ni/S15-CA, (D) La−Ni/S15-CA, (E) Fe−Ni/S15-CA, and (F) HRTEM-mapping images of the Ni/S15-CA catalyst.

characteristic peaks indexed as the (100), (110) and (200) diffractions of the SBA-15 mesostructure associated with a regular two-dimensional hexagonal structure are well reflected in all samples in Fig. S2(A),† verifying the ordered structure of all the catalysts even after loading 10 wt% Ni and 1 wt% additive metal, which is in a good agreement with the results of N_2 physisorption. In the wide-angle XRD patterns (Fig. 2(B)), the characteristic broad peak in the range of 15–30° is ascribed to the amorphous silica and strong diffraction peaks at 37.4°, 43.4° and 63.0° are assigned to the NiO particles with a face-centered cubic structure (JCPDS-ICDD No. 78-0429), which were clearly observed for all the catalysts. It is worth noting that a significant reduction in the peak intensity of Ni/S15-CA was obtained compared to that of Ni/S15, which indicates that the metal particles were significantly refined by the addition of citric acid. The average size of the NiO particles was calculated using the Scherrer equation and the full width at half maximum (FWHM) at 43.4°, and the results are shown in Table 1. The average size of the NiO particles decreases from 11.5 nm in Ni/S15 to 8.1 nm in Ni/S15-CA, and further to 7.4 nm, 7.7 nm and 7.8 nm in Mo−Ni/S15, La−Ni/S15-CA and Fe−Ni/S15-CA,
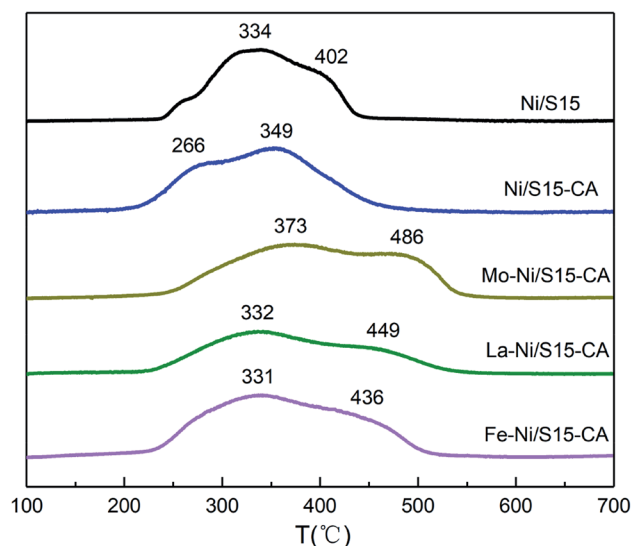

Fig. 2 H$_2$-TPR curves of the catalysts.

RSC Advances

Table 1 The NiO particle size, metal content, nickel dispersion and surface area of the catalysts

Sample	$D_{NiO}{}^a$ (nm)	Ni content[b] (mol%)	Additive metal content[b] (mol%)	Ni dispersion[c] (%)	Ni surface area[c] (m² g⁻¹ sample)
Ni/S15	11.5	9.4	—	1.6	1.1
Ni/S15-CA	8.1	10.0	—	2.9	2.6
Mo–Ni/S15-CA	7.4	10.0	1.3	3.0	2.8
La–Ni/S15-CA	7.7	9.2	0.9	3.1	2.9
Fe–Ni/S15-CA	7.8	9.7	1.0	3.0	2.8

[a] NiO particle size obtained from XRD curve and Scherrer equation. [b] Obtained by ICP analysis. [c] Obtained by H₂ pulse chemisorption.

Table 2 The adsorption properties and electronic properties of the catalysts

Samples	XPS (Ni 2p$_{3/2}$)		CO-TPD		
	BE (eV)	Ni surface concentration (%)	T (°C)	Fraction (%)	CO desorption amount (cm³ g⁻¹)
Ni/S15	855.5	1.3	330	19.4	0.72
Ni/S15-CA	855.3	1.8	298	43.2	2.14
Mo–Ni/S15-CA	855.0	2.3	310	48.8	5.62
La–Ni/S15-CA	855.0	2.1	319	47.1	4.14
Fe–Ni/S15-CA	855.1	2.0	311	44.0	3.75

respectively. With the same Ni loading content, the metal dispersion and surface area increased together with a reduction in metal particle size (seen in Table 2), which is believed to improve the catalytic activity in general. It can be inferred that the citric acid-assisted impregnation method is beneficial to enhance the performance of the catalysts, which was confirmed by the subsequent activity evaluation experiments.

3.2 Improvement in the metal-support interaction in the catalysts

The incorporation of metal promoters had a significant effect on the nature and surface exposure of nickel species, which was fully investigated by XPS, as shown in Fig. S3.† The Ni 2p spectra of the fresh catalysts are shown in Fig. S3† and the C 1s line at 284.8 eV was taken as a reference for binding energy (BE) calibration. The peaks at about 855 eV and 861 eV are attributed to the Ni 2p$_{3/2}$ main peak and Ni 2p$_{3/2}$ satellite peak, and the peaks at about 874 eV and 880 eV are assigned to the Ni 2p$_{1/2}$ main peak and Ni 2p$_{1/2}$ satellite peak, respectively.[21] It is known that there are 9.4 electrons in the 3d electronic orbit and 0.6 electrons in the 4s electronic orbits of Ni atoms. Electron–hole pairs can accept electrons from other atoms or ions. In comparison with Ni/S15, the BE of Ni 2p$_{3/2}$ in the bimetallic catalysts shifted to a lower value (shown in Table 2), indicating the occurrence of electron transfer from the second metal to Ni with an increase of in electron cloud density in the Ni atoms. It is believed that the strength of Ni–C bonds and C–O bonds in the Ni–C–O bonds are strengthened and weakened during syngas methanation, respectively, and the reducibility of NiO species can be effectively enhanced, which was confirmed by the results of the CO temperature-programmed desorption (CO-TPD) and hydrogen temperature-programmed reduction (H₂-TPR) experiments. Additionally, the Ni/S15-CA catalyst had a lower Ni 2p$_{3/2}$ BE

compare to that of Ni/S15 (855.3 eV for the Ni/S15-CA catalyst and 855.5 eV for the Ni/S15). As is known, some reducing gases (such as H₂ and CO) are generated during the decomposition of CA, which can cause a certain degree of reduction in the catalyst. Finally, the electron cloud density increased and the activity of the Ni/S15-CA catalyst in CO methanation improved, which is consistent with the subsequent experimental results of the catalytic performance evaluation.

Fig. S4† shows the adsorption performance of CO by the investigated catalysts. According to the literature,[22] CO desorbed at low temperature (100–250 °C) and high temperature (250–400 °C) are attributed to adsorbed CO, which has weak and strong interaction with the active metal, respectively, and that desorbed at high temperature is the active reactant. Table 2 illustrates the area ratio of the CO desorption peak in the temperature range of 250–400 °C. It is evident that the effective CO ratio significantly increased from 19.4% for Ni/S15 to 43.2% in Ni/S15-CA and further increased to 48.8% for Mo–Ni/S15-CA with the best CO adsorption and dissociation ability. It is well-known that a catalytic reaction can only occur when the reactant chemically adsorbs on the surface of the catalyst with an appropriate adsorption strength. Therefore, the adsorption and dissociation of CO on Ni-based catalysts are important steps in the methanation process, which determine the catalytic performance of the catalyst.[23] As a result, the incorporation of metal promoters assisted by CA caused the CO dissociation to become much easier and effectively improved the catalytic activity of the Ni-based catalysts, especially at a low temperature.

The results of H₂-TPR are shown in Fig. 2. Since NiO is reduced to Ni⁰ without going through intermediate oxides, the peaks at different temperatures should be assigned to different species. Ni/S15 shows two reduction peaks at 334 °C and 402 °C, which are ascribed to the nickel oxides possessing a weak

interaction (type I) and a strong interaction (type II) with the support, respectively. Compared with Ni/S15, the TPR pattern of Ni/S15-CA shifted toward a lower temperature, indicating the formation of amorphous NiO by the introduction of the organic additive, which could be reduced under 300 °C.[24] However, this effect can be inhibited by adding metal promoters. The reduction temperatures of the bimetallic catalyst improved significantly compared with that of Ni/S15, especially for the type II interaction, showing that the metal promoters enhanced the interaction between Ni and the support, and thus inhibited the aggregation of the nickel species under heat treatment. The maximum enhancement in the reduction temperature was obtained in the system with Mo as the metal promoter.

3.3 Catalytic activity in CO methanation

The catalytic performance of the samples in CO methanation was investigated in a fixed-bed reactor, and the results are shown in Fig. 3. The reaction temperature, pressure and space velocity was 250–500 °C, 0.1 MPa and 15 000 mL h^{-1} g^{-1}, respectively. The CO conversion for the Ni/S15 catalyst was only 30.3% at 250 °C due to the dynamic limit, which is much lower than that of the other catalysts with CO conversion above 98% even under low temperature. The better metal dispersion in the catalysts prepared by the CA-assisted impregnation method contributed to this significant improvement in catalytic performance. Among the systems, Mo–Ni/S15-CA showed the best performance at 250 °C with a CO conversion of 98.7% and CH_4 selectivity of 91.9%. However, a too high reaction temperature is not conducive to the reaction because of the huge amount of heat released in the process. Therefore, the CO conversion increased first and then decreased as the temperature increased for all the catalysts.

During the CO methanation process, the conversion of CO to CH_4 ($CO + 3H_2 = CH_4 + H_2O$) is the main reaction. There are also some side reactions such as the water gas shift (WGS) reaction ($CO + H_2O = CO_2 + H_2$) and CO disproportionation reaction ($2CO = C + CO_2$), which affect the CH_4 selectivity and CH_4 yield. By calculating the sum of unreacted CO, produced methane and CO_2, the carbon balance during the reaction

reached about 99%. Therefore, carbon dioxide is the major byproduct in the CO methanation performed on the Ni-based SBA-15 catalyst.

As illustrated in Fig. 3(B), the introduction of citric acid in the Ni/S15-CA catalyst improved its CH_4 selectivity significantly. Simultaneously, the metal promoters also enhanced the catalytic performance to some extent. By comparing the catalytic performance of Mo–Ni/S15-CA, La–Ni/S15-CA and Fe–Ni/S15-CA, it can be seen that the promotion effect of Mo was best, followed by La, and finally Fe. At the reaction temperature of 350 °C, the CO conversion of Mo–Ni/S15-CA catalyst was 100%, and the CH_4 selectivity was 94.1%. Since the large particle size of nickel could improve the WGS reaction activity,[25] the CH_4 selectivity increased with a decrease in the nickel particles size accordingly. It is well known that Fe-based materials are excellent catalysts for the WGS reaction, which prefers to produce more CO_2 during methanation.[26] This is why the CH_4 selectivity of Fe–Ni/S15-CA was lower than that of the other bimetallic catalysts.

3.4 Sintering resistance and mechanism of bimetallic catalysts

Since CO methanation is a strongly exothermic reaction, the temperature will increase sharply if the heat is not removed in time, which will lead to catalyst sintering and a decline in catalytic activity. Thus, the sintering resistance of methanation catalysts plays a crucial role in the industrial production of synthetic natural gas. To stimulate the sintering process, the catalysts were calcinated at 700 °C for 2 h in reactant gas ($n(H_2) : n(CO) = 3 : 1$, 15 000 mL min^{-1}). The sintering resistance of the catalysts was evaluated by comparing their activity at 350 °C before and after calcination, and the results are shown in Table 3. For the Mo–Ni/S15-CA catalyst, its catalytic performance remains the same, which indicates this catalyst has excellent sintering resistance. The catalytic activities of the other four catalysts all decreased to a certain extent after calcination. The decrease followed the order of La–Ni/S15-CA < Fe–Ni/S15-CA < Ni/S15-CA < Ni/S15. In general, catalysts sinter easily, and the size of the metal particles tends to increase at high temperatures due to
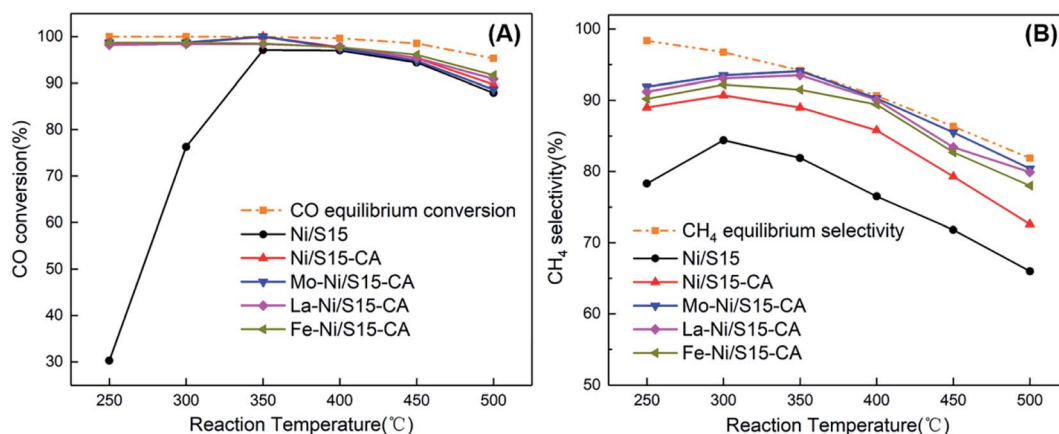

Fig. 3 Catalytic performance of the catalysts in CO methanation. (A) CO conversion; (B) CH_4 selectivity.

RSC Advances

Table 3 The catalytic performance of the catalysts before and after calcination at 700 °C for 2 h

Catalyst	Before calcination		After calcination	
	CH_4 selectivity/%	CO conversion/%	CH_4 selectivity/%	CO conversion/%
Ni/S15	84.4	76.3	46.4	23.2
Ni/S15-CA	91.7	98.6	85.1	85.7
Mo–Ni/S15-CA	93.5	98.7	93.0	98.7
La–Ni/S15-CA	93.1	98.4	91.7	96.4
Fe–Ni/S15-CA	92.2	98.7	89.6	87.8

the Ostwald ripening of metallic Ni, resulting in a reduction in catalytic activity. However, if there is a strong interaction between the metal particles and the support, it will have an inhibiting effect on the agglomeration of the particles. According to the results of H_2-TPR, it can be seen that metal promoters strengthened the interaction between nickel and the support, ultimately improving the sintering resistance of the catalysts. Although the interaction between nickel and the support in Ni/S15-CA was almost the same as that in Ni/S15, the agglomeration of metal particles at a high temperature was inhibited by the confinement effect of the support since the Ni particles were distributed in the mesochannels of the support due to the effects of CA. Consequently, the sintering resistance of Ni/S15-CA was better than that of Ni/S15.

As mentioned previously, high temperature can cause sintering of the catalyst, which leads to a decline in activity. Moreover, high heat will promote the CO disproportionation reaction ($2CO = C + CO_2$), resulting in the deposition of carbon. At a lower reaction temperature, nickel can also react with CO to form nickel carbonyl, resulting in a loss of nickel, which will affect the catalytic performance.[27] Thus, to study the mechanism of sintering resistance enhancement and the main cause of catalyst deactivation, N_2 physical adsorption, XRD, ICP, H_2 pulse chemisorption, HRTEM, elemental analysis and TG were utilized in this work.

The results of the N_2 physisorption of the support and the catalysts after calcination are listed in Table S2.† The BET surface areas of all the catalysts decreased by 20–25% with nearly unchanged average pore sizes, which is mainly due to the partial collapse of the mesoporous structure at high temperature. It is noteworthy that the BET surface area of SBA-15 was reduced by 52% after calcination at 700 °C for 2 h, which is much larger than that of all the other catalysts. It is evident that the presence of an active metal prevents the collapse of the support structure at a high temperature to some extent.

The H_2 pulse chemisorption test (Table 4) indicates that the metal dispersion of Ni/S15 decreased considerably by 62.5%. However, the metal dispersion of all the catalysts prepared via the CA-assisted impregnation method only declined by less than 15%, especially the used Mo–Ni/S15-CA catalyst showed no loss in metal dispersion. Therefore, the activity reduction in the catalyst may be mainly attributed to the metal dispersion. The Ni and additive metal contents of the used catalyst after calcination were also obtained by ICP, as shown in Table 4. The similarity between the Ni content of the fresh catalysts (Table 1) and the used catalysts after calcination shows that there was no loss of metals during the reaction.

The catalyst structure and the Ni particle size after calcination were investigated using XRD and the results are shown in Fig. S5.† The characteristic diffraction peaks of SBA-15 and amorphous SiO_2 can be clearly observed in the patterns, indicating the stability of the ordered structure of the support. The characteristic peaks of metallic Ni shifted to 44.5°, 51.8° and 76.4°. According to the calculation based on the Scherrer equation, the Ni particle size in the Ni/S15 catalyst is 19.3 nm, which is much higher than the NiO particle size (11.5 nm) of the fresh catalyst. It is believed that the size increase of the NiO particle size by sintering should be the reason for the decrease in the number of active sites, eventually resulting in the deactivation of the catalyst. However, the diffraction peak strength of the Ni particles was too weak to calculate the average particle size for the other catalysts. The agglomeration of nickel particles in the used Ni/S15 was also observed by HRTEM, as displayed in Fig. 4. In contrast, the metal particles of the catalysts prepared by the CA-assisted impregnation method were still dispersed uniformly in the channels of the support even after calcination at 700 °C. Thus, it can be concluded that the confinement effect of the channel and the strong interaction between the metal and support inhibited the agglomeration of

Table 4 The metal content, nickel dispersion and surface area of the used catalysts after calcination

Samples	Ni content[a] (mol%)	Additive metal content[a] (mol%)	Ni dispersion[b] (%)	Ni surface area[b] ($m^2 g^{-1}$ sample)
Ni/S15	9.5	—	0.6	0.5
Ni/S15-CA	10.0	—	2.5	2.2
Mo–Ni/S15-CA	9.9	1.0	3.1	2.9
La–Ni/S15-CA	9.0	0.9	3.0	2.8
Fe–Ni/S15-CA	9.2	1.2	2.7	2.5

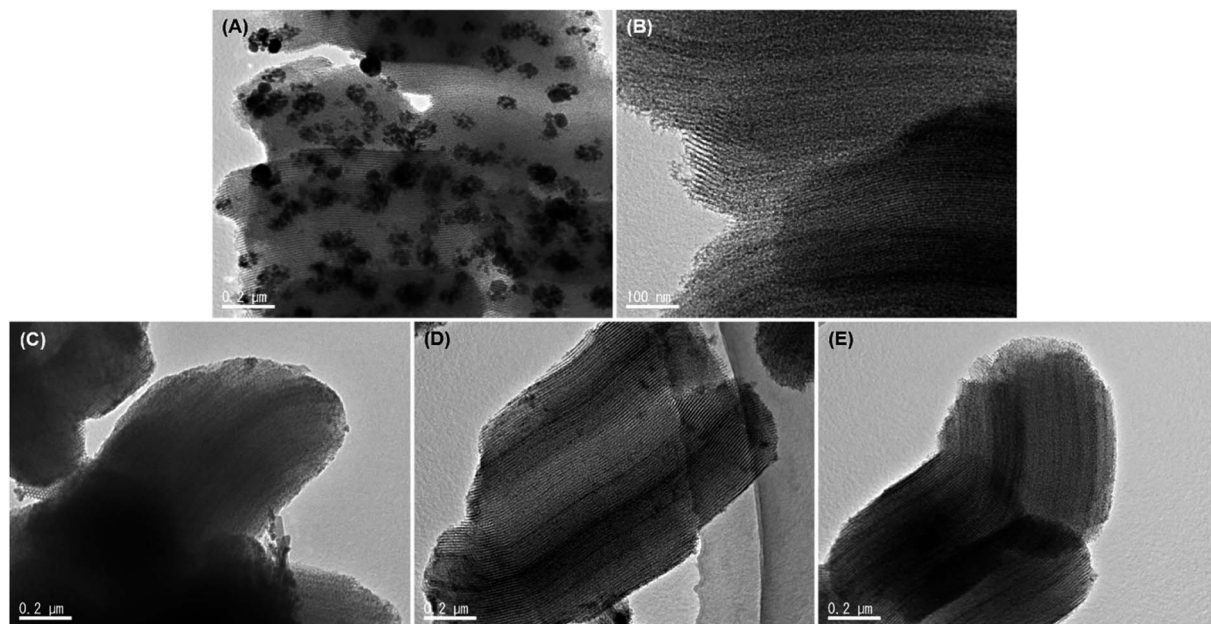[a] Obtained by ICP analysis. [b] Obtained by H_2 pulse chemisorption.

Fig. 4 HRTEM images of the used catalysts after calcination. (A) Ni/S15, (B) Ni/S15-CA, (C) Mo−Ni/S15-CA, (D) La−Ni/S15-CA, and (E) Fe−Ni/S15-CA.

nickel, which ultimately displayed excellent sintering resistance in the CO methanation.

TG analysis under an air atmosphere and elemental analysis were used to characterize the carbon species and carbon amount of the used catalysts after calcination. Fig. 5 shows the TG profiles of the used catalysts after calcination. The weight loss that occurred below 150 °C was caused by the volatilization of the moisture and impurities and the weight increased with the oxidation of metallic Ni in the air. Generally, three types of carbonaceous species are identified over nickel-based catalysts, namely C_α (150–450 °C), C_β (450–650 °C) and C_γ (>650 °C).[28] Specifically, only C_α and C_β were deposited on all the catalysts. The total carbon amounts were the weight loss of the catalysts

Table 5 The carbon amount of the used catalysts after calcination

Sample	Carbon amount (wt%)			
	Before reaction[a]	After reaction[a]	ΔW	After reaction[b]
Ni/S15	0.89	2.68	1.79	2.16
Ni/S15-CA	0.97	4.15	3.18	4.66
Mo–Ni/S15-CA	0.87	3.06	2.19	3.61
La–Ni/S15-CA	0.99	5.32	4.33	5.64
Fe–Ni/S15-CA	0.96	5.28	4.32	5.46

[a] Obtained by elemental analysis. [b] Obtained by TG.
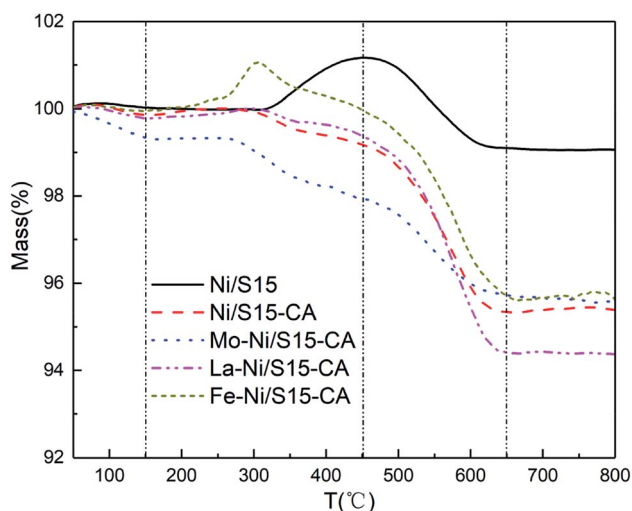
above 150 °C, and the calculated results are shown in Table 5. There was about 0.9 wt% carbon species in the fresh catalysts, which may have come from TEOS during the calcination. Comparing the catalytic performance and carbon amounts of La-Ni/S15-CA and Fe-Ni/S15-CA catalysts, the decline in activity for Fe-Ni/S15-CA was larger than that of La-Ni/S15-CA, while the carbon deposition amounts were almost the same. Similarly, the decrease in catalytic activity for the Ni/S15 catalyst was the largest, but its carbon amount was the smallest. Therefore, a small amount of carbon deposition is not the main reason for the catalyst deactivation in syngas methanation. According to the above experimental results, it can be proposed that the improvement in sintering resistance is attributed to the confinement effect of the support and the strong interaction between the metal and support.

4 Conclusions

In this work, the effect of citric acid and additive metals (Mo, La and Fe) on the physicochemical properties and catalytic

Fig. 5 TG profiles of the used catalysts after calcination.

performance of nickel-based SBA-15 for CO methanation in a fixed-bed reactor were studied. The introduction of additive metals improved the surface nickel concentration and the electron cloud density of Ni atoms, which effectively enhanced the low-temperature catalytic activity. In addition, citric acid promoted the dispersion of metals in the mesochannels of SBA-15. The Mo–Ni/S15-CA catalyst exhibited the highest low-temperature catalytic activity among the catalysts. At the reaction temperature of 250 °C, the CO conversion and CH_4 selectivity of the Mo–Ni/S5-CA catalyst reached 98.7% and 91.9%, respectively. Moreover, the catalytic activity of Mo–Ni/S15-CA remained almost the same after calcination at 700 °C for 2 h because of the synergetic effect of the enhancement of the metal-support interaction and the confinement effect of the support, showing a significant improvement in sintering resistance.

Conflicts of interest

There are no conflicts to declare.

Acknowledgements

References

1 L. Wang, F. Zhang, E. Pilot, *et al.* Taking Action on Air Pollution Control in the Beijing-Tianjin-Hebei Region: Progress, Challenges and Opportunities, *Int. J. Environ. Res. Publ. Health*, 2018, **15**(2), 1–27.

2 M. E. Bildirici and T. Bakirtas, The Relationship among Oil, Natural Gas and Coal Consumption and Economic Growth in Brics (Brazil, Russian, India, China, Turkey And south Africa) Countries, *Energy*, 2014, **65**, 134–144.

3 L. Romano, F. Ruggeri and R. Marx, Sng Production from Coal: A Possible Solution to Energy Demand, *Energy Procedia*, 2014, **45**, 1330–1336.

4 B.-Y. Yu and I. L. Chien, Design and Economic Evaluation of a Coal-to-Synthetic Natural Gas Process, *Ind. Eng. Chem. Res.*, 2015, **54**(8), 2339–2352.

5 J. Gao, Q. Liu, F. Gu, *et al.* Recent Advances in Methanation Catalysts for the Production of Synthetic Natural Gas, *RSC Adv.*, 2015, **5**(29), 22759–22776.

6 I. Czekaj, F. Loviat, F. Raimondi, *et al.* Characterization of Surface Processes at the Ni-Based Catalyst During the Methanation of Biomass-Derived Synthesis Gas: X-Ray Photoelectron Spectroscopy (Xps), *Appl. Catal., A*, 2007, **329**, 68–78.

7 Y.-Z. Wang, F.-M. Li, H.-M. Cheng, *et al.* A Comparative Study on the Catalytic Properties of High Ni-Loading Ni/SiO₂ and Low Ni-Loading Ni-Ce/SiO₂ for Co Methanation, *J. Fuel Chem. Technol.*, 2013, **41**(8), 972–977.

8 S. Rönsch, J. Schneider, S. Matthischke, *et al.* Review on Methanation - from Fundamentals to Current Projects, *Fuel*, 2016, **166**, 276–296.

9 S. Li, X. Ji, X. Zhang, *et al.* Coal to Sng: Technical Progress, Modeling and System Optimization through Exergy Analysis, *Appl. Energy*, 2014, **136**, 98–109.

10 T. T. M. Nguyen, L. Wissing and M. S. Skjøth-Rasmussen, High Temperature Methanation: Catalyst Considerations, *Catal. Today*, 2013, **215**, 233–238.

11 M. Tao, X. Meng, Y. Lv, *et al.* Effect of Impregnation Solvent on Ni Dispersion and Catalytic Properties of Ni/SBA-15 for CO Methanation Reaction, *Fuel*, 2016, **165**, 289–297.

12 B. Liu, N. Yao, S. Li, *et al.* Methanation of CO in Hydrogen-Rich Gas on Ni–Ru/SiO₂ Catalyst: The Type of Active Sites and Ni–Ru Synergistic Effect, *Chem. Eng. J.*, 2016, **304**, 476–484.

13 C. Cheng, D. Shen, R. Xiao, *et al.* Methanation of Syngas (H₂/Co) over the Different Ni-Based Catalysts, *Fuel*, 2017, **189**, 419–427.

14 F. Meng, X. Li, M. Li, *et al.* Catalytic Performance of CO Methanation over La-Promoted Ni/Al₂O₃ Catalyst in a Slurry-Bed Reactor, *Chem. Eng. J.*, 2017, **313**, 1548–1555.

15 F. Meng, Z. Li, J. Liu, *et al.* Effect of Promoter Ce on the Structure and Catalytic Performance of Ni/Al₂O₃ Catalyst for CO Methanation in Slurry-Bed Reactor, *J. Nat. Gas Sci. Eng.*, 2015, **23**, 250–258.

16 S. Tada, R. Kikuchi, A. Takagaki, *et al.* Effect of Metal Addition to Ru/TiO₂ Catalyst on Selective CO Methanation, *Catal. Today*, 2014, **232**, 16–21.

17 J. Zhang, Z. Xin, X. Meng, *et al.* Effect of MoO₃ on the Heat Resistant Performances of Nickel Based MCM-41 Methanation Catalysts, *Fuel*, 2014, **116**, 25–33.

18 Y. Lv, Z. Xin, X. Meng, *et al.* Effect of La, Mg and Mo Additives on Dispersion and Thermostability of Ni Species on KIT-6 for CO Methanation, *Appl. Catal., A*, 2017, **543**, 125–132.

19 S. Hwang, U. G. Hong, J. Lee, *et al.* Methanation of Carbon Dioxide over Mesoporous Nickel-M-Alumina (M = Fe, Zr, Ni, Y, and Mg) Xerogel Catalysts: Effect of Second Metal, *Catal. Lett.*, 2012, **142**(7), 860–868.

20 D. Zhao, J. Sun, Q. Li, *et al.* Morphological Control of Highly Ordered Mesoporous Silica SBA-15, *Chem. Mater.*, 2000, **12**(2), 275–279.

21 Q. Liu, F. Gu, X. Lu, *et al.* Enhanced Catalytic Performances of Ni/Al₂O₃ Catalyst Via Addition of V₂O₃ for CO Methanation, *Appl. Catal., A*, 2014, **488**, 37–47.

22 B. Lu and K. Kawamoto, Direct Synthesis of Highly Loaded and Well-Dispersed NiO/SBA-15 for Producer Gas Conversion, *RSC Adv.*, 2012, **2**(17), 6800–6805.

23 J. Sehested, S. Dahl, J. Jacobsen, *et al.* Methanation of CO over Nickel: Mechanism and Kinetics at High H₂/CO Ratios, *J. Phys. Chem. B*, 2005, **109**(6), 2432–2438.

24 M. Tao, Z. Xin, X. Meng, *et al.* Highly Dispersed Nickel within Mesochannels of SBA-15 for CO Methanation with Enhanced Activity and Excellent Thermostability, *Fuel*, 2017, **188**, 267–276.

25 G. Zhang, T. Sun, J. Peng, *et al.* A Comparison of Ni/SiC and Ni/Al$_2$O$_3$ Catalyzed Total Methanation for Production of Synthetic Natural Gas, *Appl. Catal., A*, 2013, **462–463**, 75–81.

26 C. Rhodes, G. J. Hutchings and A. M. Ward, Water-Gas Shift Reaction: Finding the Mechanistic Boundary, *Catal. Today*, 1995, **23**(1), 43–58.

27 J. Sehested, Four Challenges for Nickel Steam-Reforming Catalysts, *Catal. Today*, 2006, **111**(1), 103–110.

28 D. Tian, Z. Liu, D. Li, *et al.* Bimetallic Ni-Fe Total-Methanation Catalyst for the Production of Substitute Natural Gas under High Pressure, *Fuel*, 2013, **104**, 224–229.